Monthly Notices
of the
ROYAL ASTRONOMICAL SOCIETY

MNRAS **459,** 3203–3216 (2016)
Advance Access publication 2016 April 15

doi:10.1093/mnras/stw861

Galaxy bias from the Dark Energy Survey Science Verification data: combining galaxy density maps and weak lensing maps

C. Chang,[1⋆] A. Pujol,[2] E. Gaztañaga,[2] A. Amara,[1] A. Réfrégier,[1] D. Bacon,[3] M. R. Becker,[4,5] C. Bonnett,[6] J. Carretero,[2,6] F. J. Castander,[2] M. Crocce,[2] P. Fosalba,[2] T. Giannantonio,[7,8,9] W. Hartley,[1] M. Jarvis,[10] T. Kacprzak,[1] A. J. Ross,[11] E. Sheldon,[12] M. A. Troxel,[13] V. Vikram,[14] J. Zuntz,[13] T. M. C. Abbott,[15] F. B. Abdalla,[16,17] S. Allam,[18] J. Annis,[18] A. Benoit-Lévy,[16,19,20] E. Bertin,[19,20] D. Brooks,[16] E. Buckley-Geer,[18] D. L. Burke,[5,21] D. Capozzi,[3] A. Carnero Rosell,[22,23] M. Carrasco Kind,[24,25] C. E. Cunha,[5] C. B. D'Andrea,[3,26] L. N. da Costa,[22,23] S. Desai,[27,28] H. T. Diehl,[18] J. P. Dietrich,[27,28] P. Doel,[16] T. F. Eifler,[10,29] J. Estrada,[18] A. E. Evrard,[30,31] B. Flaugher,[18] J. Frieman,[18,32] D. A. Goldstein,[33,34] D. Gruen,[5,21,27,35] R. A. Gruendl,[24,25] G. Gutierrez,[18] K. Honscheid,[11,36] B. Jain,[10] D. J. James,[15] K. Kuehn,[37] N. Kuropatkin,[18] O. Lahav,[16] T. S. Li,[38] M. Lima,[22,39] J. L. Marshall,[38] P. Martini,[11,36] P. Melchior,[40] C. J. Miller,[30,31] R. Miquel,[6,41] J. J. Mohr,[27,28,35] R. C. Nichol,[3] B. Nord,[18] R. Ogando,[22,23] A. A. Plazas,[29] K. Reil,[21] A. K. Romer,[42] A. Roodman,[5,21] E. S. Rykoff,[5,21] E. Sanchez,[43] V. Scarpine,[18] M. Schubnell,[31] I. Sevilla-Noarbe,[24,43] R. C. Smith,[15] M. Soares-Santos,[18] F. Sobreira,[18,22] E. Suchyta,[10] M. E. C. Swanson,[25] G. Tarle,[31] D. Thomas[3] and A. R. Walker[15]

Affiliations are listed at the end of the paper

Accepted 2016 April 12. Received 2016 April 11; in original form 2016 January 1

ABSTRACT

We measure the redshift evolution of galaxy bias for a magnitude-limited galaxy sample by combining the galaxy density maps and weak lensing shear maps for a $\sim$116 deg^2 area of the Dark Energy Survey (DES) Science Verification (SV) data. This method was first developed in Amara et al. and later re-examined in a companion paper with rigorous simulation tests and analytical treatment of tomographic measurements. In this work we apply this method to the DES SV data and measure the galaxy bias for a $i < 22.5$ galaxy sample. We find the galaxy bias and 1σ error bars in four photometric redshift bins to be 1.12 ± 0.19 ($z = 0.2$–0.4), 0.97 ± 0.15 ($z = 0.4$–0.6), 1.38 ± 0.39 ($z = 0.6$–0.8), and 1.45 ± 0.56 ($z = 0.8$–1.0). These measurements are consistent at the 2σ level with measurements on the same data set using galaxy clustering and cross-correlation of galaxies with cosmic microwave background lensing, with most of the redshift bins consistent within the 1σ error bars. In addition, our method provides the only σ_8 independent constraint among the three. We forward model the main observational effects using mock galaxy catalogues by including shape noise, photo-z errors, and masking effects. We show that our bias measurement from the data is consistent

⋆ E-mail: chihway.chang@phys.ethz.ch

with that expected from simulations. With the forthcoming full DES data set, we expect this method to provide additional constraints on the galaxy bias measurement from more traditional methods. Furthermore, in the process of our measurement, we build up a 3D mass map that allows further exploration of the dark matter distribution and its relation to galaxy evolution.

Key words: gravitational lensing: weak – surveys – large-scale structure of Universe.

1 INTRODUCTION

Galaxy bias is one of the key ingredients for describing our observable Universe. In a concordance Λ cold dark matter (ΛCDM) model, galaxies form at overdensities of the dark matter distribution, suggesting the possibility of simple relations between the distribution of galaxies and dark matter. This particular relation is described by a galaxy bias model (Kaiser 1984). Galaxy bias bridges the observable Universe of galaxies with the underlying dark matter. For a full review of literature on galaxy bias, we refer the readers to Eriksen & Gaztanaga (2015) and references therein.

Observationally, several measurement techniques exist for constraining galaxy bias. The most common approach is to measure galaxy bias through the two-point correlation function (2PCF) of galaxies (Blake, Collister & Lahav 2008; Cresswell & Percival 2009; Simon et al. 2009; Zehavi et al. 2011; Coupon et al. 2012). Counts-in-cells (CiC) is another method where the higher moments of the galaxy probability density function (PDF) are used to constrain galaxy bias (Blanton 2000; Wild et al. 2005; Swanson et al. 2008). Alternatively, one can combine galaxy clustering with measurements from gravitational lensing, which probes the total (baryonic and dark) matter distribution. Such measurements include combining galaxy clustering with galaxy–galaxy lensing (Simon et al. 2007; Jullo et al. 2012; Mandelbaum et al. 2013) and lensing of the cosmic microwave background (CMB; Schneider 1998; Giannantonio et al. 2016). The method we present in this work also belongs to this class.

With ongoing and upcoming large galaxy surveys (the Hyper SuprimeCam,[1] the Dark Energy Survey,[2] the Kilo Degree Survey,[3] the Large Synoptic Survey Telescope,[4] the *Euclid* mission,[5] the Wide-Field Infrared Survey Telescope[6]), statistical uncertainties on the galaxy bias measurements will decrease significantly. It is thus interesting to explore alternative and independent options of measuring galaxy bias. Such measurements would be powerful tests for systematic uncertainties and break possible degeneracies.

In this paper, we present a new measurement of the redshift-dependent galaxy bias from the Dark Energy Survey (DES) Science Verification (SV) data using a novel method. Our method relies on the cross-correlation between weak lensing shear and galaxy density maps to constrain galaxy bias. The method naturally combines the power of galaxy surveys and weak lensing measurements in a way that only weakly depends on assumptions of the cosmological parameters. In addition, the method involves building up a high-resolution 3D mass map in the survey volume which is interesting for studies of the dark matter distribution at the map level. The relation between the galaxy sample and the mass map also provides information for studies of galaxy evolution.

[1] www.naoj.org/Projects/HSC
[2] www.darkenergysurvey.org
[3] kids.strw.leidenuniv.nl
[4] www.lsst.org
[5] sci.esa.int/euclid
[6] wfirst.gsfc.nasa.gov

The analysis in this paper closely follows Amara et al. (2012, hereafter A12) and Pujol et al. (2016, hereafter Paper I). A12 applied this method to Cosmological Evolution Survey (COSMOS) and zCOSMOS data and discussed different approaches for constructing the galaxy density map and galaxy bias. Paper I carried out a series of simulation tests to explore the regime of the measurement parameters where the method is consistent with 2PCF measurements, while introducing alternative approaches to the methodology. Building on these two papers, this work applies the method to the DES SV data, demonstrating the first constraints with this method using photometric data. Simulations are used side-by-side with data to ensure that each step in the data analysis is robust. In particular, we start with the same set of 'ideal' simulations used in Paper I and gradually degrade until they match the data by including noise, photometric redshift errors, and masking effects.

The paper is organized as follows. In Section 2 we overview the basic principles of our measurement method. In Section 3 we introduce the data and simulations used in this work. The analysis and results are presented in Section 4, first with a series of simulation tests and then with the DES SV data. We also present a series of systematics tests here. In Section 5 we compare our measurements with bias measurements on the same data set using different approaches. We conclude in Section 6.

2 BACKGROUND THEORY

2.1 Linear galaxy bias

In this work we follow Paper I, where the overdensities of galaxies δ_g is linearly related to the overdensities of dark matter δ at some given smoothing scale R, or

$$\delta_g(z, R) = b(z, R)\delta(z, R). \quad (1)$$

We define $\delta \equiv \frac{\rho-\bar{\rho}}{\bar{\rho}}$, where ρ is the dark matter density and $\bar{\rho}$ is the mean dark matter density at a given redshift. δ_g is defined similarly, with ρ replaced by ρ_g, the number density of galaxies. b can depend on galaxy properties such as luminosity, colour, and type (Swanson et al. 2008; Cresswell & Percival 2009). This definition is often referred to as the 'local bias' model. According to Manera & Gaztañaga (2011), at sufficiently large scales ($\gtrsim$40 Mpc h^{-1} comoving distance), $b(z, R)$ in equation (1) is consistent with galaxy bias defined through the 2PCF of dark matter (ξ_{dm}) and galaxies (ξ_g). That is, the following equation holds:

$$\xi_g(r) = \langle\delta_g(\boldsymbol{r_0})\delta_g(\boldsymbol{r_0}+\boldsymbol{r})\rangle = b^2\langle\delta(\boldsymbol{r_0})\delta(\boldsymbol{r_0}+\boldsymbol{r})\rangle = b^2\xi_{dm}(r), \quad (2)$$

where $\boldsymbol{r_0}$ and $\boldsymbol{r_0}+\boldsymbol{r}$ are two positions on the sky separated by vector $\boldsymbol{r}$. The angle bracket $\langle\rangle$ averages over all pairs of positions on the sky separated by distance $|\boldsymbol{r}| \equiv r$. Our work will be based on scales in this regime.

2.2 Weak lensing

Weak lensing refers to the coherent distortion, or 'shear' of galaxy images caused by large-scale cosmic structures between these

galaxies and the observer. Weak lensing probes directly the total mass instead of a proxy of the total mass (e.g. stellar mass, gas mass). For a detailed review of the theoretical background of weak lensing, see e.g. Bartelmann & Schneider (2001).

The main weak lensing observable is the complex shear $\boldsymbol{\gamma} = \gamma_1 + \mathrm{i}\gamma_2$, which is estimated by the measured shape of galaxies. The cosmological shear signal is much weaker than the intrinsic galaxy shapes. The uncertainty in the shear estimate due to this intrinsic galaxy shape is referred to as 'shape noise', and is often the largest source of uncertainty in lensing measurements. Shear can be converted to convergence, κ, a scalar field that directly measures the projected mass. The convergence at a given position $\boldsymbol{\theta}$ on the sky can be expressed as

$$\kappa(\boldsymbol{\theta}, p_\mathrm{s}) = \int_0^\infty \mathrm{d}\chi\, q(\chi, p_\mathrm{s})\delta(\boldsymbol{\theta}, \chi), \tag{3}$$

where $q(\chi, p_\mathrm{s})$ is the lensing weight:

$$q(\chi, p_\mathrm{s}) \equiv \frac{3H_0^2\Omega_\mathrm{m}\chi}{2c^2a(\chi)} \int_\chi^\infty \mathrm{d}\chi_\mathrm{s} \frac{\chi_\mathrm{s} - \chi}{\chi_\mathrm{s}} p_\mathrm{s}(\chi_\mathrm{s}). \tag{4}$$

Here, χ is the comoving distance, Ω_m is the total matter density of the Universe today normalized by the critical density today, H_0 is the Hubble constant today, and a is the scale factor. $p_\mathrm{s}(\chi)$ is the normalized redshift distribution of the 'source' galaxy sample where the lensing quantities ($\boldsymbol{\gamma}$ or κ) are measured. In the simple case of a single source redshift plane at χ_s, p_s is a δ function and the lensing weight becomes

$$q(\chi, \chi_\mathrm{s}) \equiv \frac{3H_0^2\Omega_\mathrm{m}}{2c^2a(\chi)} \frac{\chi(\chi_\mathrm{s} - \chi)}{\chi_\mathrm{s}}. \tag{5}$$

In the flat-sky approximation, conversion between $\boldsymbol{\gamma}$ and κ in Fourier space follows (Kaiser & Squires 1993, KS conversion):

$$\tilde{\kappa}(\boldsymbol{\ell}) - \tilde{\kappa_0} = D^*(\boldsymbol{\ell})\tilde{\boldsymbol{\gamma}}(\boldsymbol{\ell}); \quad \tilde{\boldsymbol{\gamma}}(\boldsymbol{\ell}) - \tilde{\boldsymbol{\gamma}}_0 = D(\boldsymbol{\ell})\tilde{\kappa}(\boldsymbol{\ell}), \tag{6}$$

where '$\tilde{X}$' indicates the Fourier transform of the field X, $\boldsymbol{\ell}$ is the spatial frequency, $\tilde{\kappa_0}$ and $\tilde{\boldsymbol{\gamma}}_0$ are small constant offsets which cannot be reconstructed and are often referred to as the 'mass-sheet degeneracy'. D is a combination of second moments of $\boldsymbol{\ell}$:

$$D(\boldsymbol{\ell}) = \frac{\ell_1^2 - \ell_2^2 + \mathrm{i}2\ell_1\ell_2}{|\boldsymbol{\ell}|^2}. \tag{7}$$

In this work we follow the implementation of equation (6) as described in Vikram et al. (2015) and Chang et al. (2015) to construct κ and $\boldsymbol{\gamma}$ maps as needed.

2.3 κ_g: a convergence template from galaxies

Following the same approach as A12 and Paper I, we now define κ_g by substituting δ with δ_g in equation (3), or

$$\kappa_\mathrm{g}(\boldsymbol{\theta}, p_\mathrm{s}) = \int_0^\infty \mathrm{d}\chi\, q(\chi, p_\mathrm{s})\delta_\mathrm{g}(\boldsymbol{\theta}, \chi). \tag{8}$$

Physically, κ_g is a 'template' for the convergence κ. In particular, in the case of a constant galaxy bias b, where $\delta_\mathrm{g} = b\delta$ everywhere, equation (8) trivially gives $\kappa_\mathrm{g} = b\kappa$. The relation between κ, κ_g, and b in the case of redshift-dependent galaxy bias (equation 1) becomes more complicated. This requires the introduction of the 'partial' κ_g, or κ_g' below. Alternatively, one can adopt the approach used in A12 and include a parametrized galaxy bias model in constructing κ_g.

To construct κ_g', instead of integrating over all foreground 'lens' galaxies in equation (8), we only consider the part of the template contributed by a given lens sample. This gives

$$\begin{aligned}\kappa_\mathrm{g}'(\boldsymbol{\theta}, \phi', p_\mathrm{s}) &= \int_0^\infty \mathrm{d}\chi\, q(\chi, p_\mathrm{s})\phi'(\chi)\delta_\mathrm{g}(\boldsymbol{\theta}, \chi) \\ &= \int_0^\infty \mathrm{d}\chi\, q(\chi, p_\mathrm{s})\phi'(\chi)\left(\frac{\rho_\mathrm{g}(\boldsymbol{\theta}, \chi)}{\bar{\rho}_\mathrm{g}(\chi)} - 1\right),\end{aligned} \tag{9}$$

where $\phi'(\chi)$ is the radial selection function of the lens sample of interest. ρ_g is the number of galaxies per unit volume and $\bar{\rho}_\mathrm{g}$ is the mean of ρ_g at a given redshift. $\phi'(\chi)$ is different from $p'(\chi)$ in equation (20) of Paper I only by a normalization: $\int \mathrm{d}\chi p'(\chi) = 1$, while $\phi'(\chi)$ integrates to a length, which is the origin of the $\Delta\chi'$ in equation (20) in Paper I. We choose to use $\phi'(\chi)$ here to facilitate the derivation later, but note that equation (14) below is fully consistent with equation (20) in Paper I. Similarly we define also a partial κ field, which we will later use in Section 2.4,

$$\kappa'(\boldsymbol{\theta}, \phi', p_\mathrm{s}) = \int_0^\infty \mathrm{d}\chi\, q(\chi, p_\mathrm{s})\phi'(\chi)\delta(\boldsymbol{\theta}, \chi). \tag{10}$$

In practice, when constructing κ_g', we assume a fixed source redshift $\bar{\chi}_\mathrm{s}$ and take the mean lensing weight $\bar{q}'$ and $\bar{\rho}_\mathrm{g}$ outside the integration of equation (9). This approximation holds in the case where q and $\bar{\rho}_\mathrm{g}$ are slowly varying over the extent of ϕ', which is true for the intermediate redshift ranges we focus on. We have

$$\kappa_\mathrm{g}'(\boldsymbol{\theta}, \phi', \bar{\chi}_\mathrm{s}) \approx \Delta\chi'\bar{q}'(\bar{\chi}_\mathrm{s})\left(\frac{\int_0^\infty \mathrm{d}\chi\phi'(\chi)\rho_\mathrm{g}(\boldsymbol{\theta}, \chi)}{\bar{\rho}_\mathrm{g}\Delta\chi'} - 1\right), \tag{11}$$

where

$$\Delta\chi' = \int_0^\infty \mathrm{d}\chi\phi'(\chi). \tag{12}$$

We further simplify the expression by defining the partial 2D surface density Σ' and $\bar{\Sigma}'$, where

$$\Sigma' = \int_0^\infty \mathrm{d}\chi\phi'(\chi)\rho_\mathrm{g}(\boldsymbol{\theta}, \chi), \quad \bar{\Sigma}' = \int_0^\infty \mathrm{d}\chi\phi'(\chi)\bar{\rho}_\mathrm{g}. \tag{13}$$

Equation (11) then becomes

$$\kappa_\mathrm{g}'(\boldsymbol{\theta}, \phi', \bar{\chi}_\mathrm{s}) \approx \Delta\chi'\bar{q}'(\bar{\chi}_\mathrm{s})\left(\frac{\Sigma'(\boldsymbol{\theta})}{\bar{\Sigma}'(\boldsymbol{\theta})} - 1\right), \tag{14}$$

which is what we measure as described in Section 4.1.

2.4 Bias estimation from the galaxy density field and the weak lensing field

The information of galaxy bias can be extracted through the cross- and autocorrelation of the κ and κ_g' fields. (In the case of constant bias, we can replace κ_g' by κ_g in all equations below.) Specifically, we calculate

$$b' = \frac{\langle\kappa_\mathrm{g}'\kappa_\mathrm{g}'\rangle}{\langle\kappa_\mathrm{g}'\kappa\rangle} = \frac{\langle\kappa_\mathrm{g}'(\boldsymbol{\theta}, \phi', \bar{\chi}_\mathrm{s})\kappa_\mathrm{g}'(\boldsymbol{\theta}, \phi', \bar{\chi}_\mathrm{s})\rangle}{\langle\kappa_\mathrm{g}'(\boldsymbol{\theta}, \phi', \bar{\chi}_\mathrm{s})\kappa(\boldsymbol{\theta}, p_\mathrm{s})\rangle}, \tag{15}$$

where $\langle\rangle$ represents a zero-lag correlation between the two fields in the brackets, averaged over a given aperture R. We can write for the most general case,

$$\langle\kappa_\mathrm{A}\kappa_\mathrm{B}\rangle = \frac{4\pi}{\pi^2R^4}\int_0^R \mathrm{d}r_1 r_1 \int_0^R \mathrm{d}r_2 r_2 \int_0^\pi \mathrm{d}\eta\omega_\mathrm{AB}(\Theta), \tag{16}$$

where κ_A and κ_B can be any of the following: $(\kappa, \kappa', \kappa_\mathrm{g}, \kappa_\mathrm{g}')$, $\Theta^2 = r_1^2 + r_2^2 - 2r_1r_2\cos\eta$, and $\omega_\mathrm{AB}(\Theta)$ is the projected two-point angular correlation function between the two fields, defined

$$\omega_\mathrm{AB}(\Theta) = \int_0^\infty \mathrm{d}\chi_\mathrm{A} \int_0^\infty \mathrm{d}\chi_\mathrm{B} q_\mathrm{A}q_\mathrm{B}\phi_\mathrm{A}'\phi_\mathrm{B}'\xi_{\kappa_\mathrm{A}\kappa_\mathrm{B}}(r), \tag{17}$$

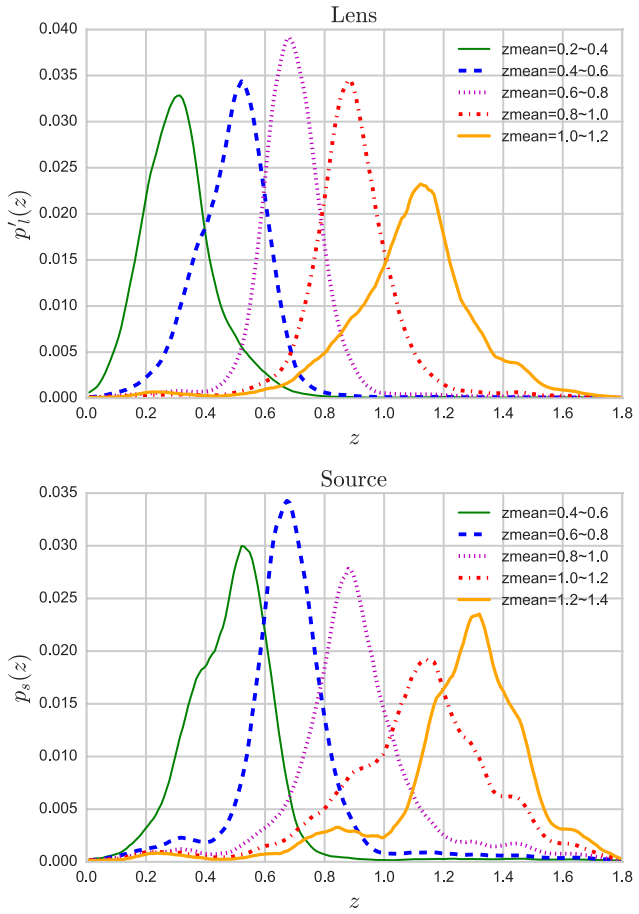

Figure 1. Normalized redshift distribution of the lens (top) and source (bottom) samples as estimated from the photo-z code SKYNET. Each curve represents the stacked PDF for all galaxies in the photo-z bin determined by $z_{\rm mean}$ as listed in the labels.

where $q_{\rm A}$ ($q_{\rm B}$) and $\phi'_{\rm A}$ ($\phi'_{\rm B}$) are the lensing weight and lens redshift selection function associated with the fields $\kappa_{\rm A}$ ($\kappa_{\rm B}$). $\xi_{\kappa_{\rm A}\kappa_{\rm B}}(r)$ is the 3D two-point correlation function. In the case of $\kappa_{\rm A} = \kappa_{\rm B} = \kappa$, $\xi_{\kappa_{\rm A}\kappa_{\rm B}}$ reduces to $\xi_{\rm dm}$ in equation (2).

For infinitely thin redshift bins, or constant bias, b' in equation (15) directly measures the galaxy bias b of the lens. However, once the lens and source samples span a finite redshift range (see e.g. Fig. 1), b' is a function of the source and lens distribution and is different from b by some factor $f(\phi', p_{\rm s})$, so that

$$b' = f(\phi', p_{\rm s})b. \tag{18}$$

Note that f can be determined if $b(z)$ is known. Since we have $b(z) = 1$ for the case of dark matter, we can calculate f by calculating b' and setting $b(z) = 1$, or

$$f(\phi', p_{\rm s}) = \frac{\langle\kappa'\kappa'\rangle}{\langle\kappa'\kappa\rangle} = \frac{\langle\kappa'(\boldsymbol{\theta}, \phi', \bar{\chi}_{\rm s})\kappa'(\boldsymbol{\theta}, \phi', \bar{\chi}_{\rm s})\rangle}{\langle\kappa'(\boldsymbol{\theta}, \phi', \bar{\chi}_{\rm s})\kappa(\boldsymbol{\theta}, p_{\rm s})\rangle}, \tag{19}$$

where κ' is defined in equation (10) and follows the same assumptions in equation (14), where the lensing weight depends on only the mean distance to the source sample $\bar{\chi}_{\rm s}$. f here corresponds to f_2 in equation (26) in Paper I. Table 1 shows an example of the f values calculated from the data.

Table 1. f factor (equation 19) calculated from data. f depends on the specific sample that is used. In this table we list numbers only for the main measurement in Section 4.4, where the NGMIX shear catalogue and the SKYNET photo-z catalogue is used.

Source redshift	Lens redshift 0.2–0.4	0.4–0.6	0.6–0.8	0.8–1.0
0.4–0.6	0.61	–	–	–
0.6–0.8	0.61	0.58	–	–
0.8–1.0	0.61	0.59	0.67	–
1.0–1.2	0.62	0.60	0.72	0.53

We use a slightly different estimator for b' compared to equation (15) in practice. Combined with equation (18), our estimator for galaxy bias is

$$b = \frac{1}{\mu}, \tag{20}$$

$$\mu = f\frac{\langle\gamma'_{\alpha,{\rm g}}\gamma'_{\alpha}\rangle}{\langle\gamma'_{\alpha,{\rm g}}\gamma'_{\alpha,{\rm g}}\rangle - \langle\gamma'^{N}_{\alpha,{\rm g}}\gamma'^{N}_{\alpha,{\rm g}}\rangle}, \tag{21}$$

with $\alpha = 1, 2$ referring to the two components of $\boldsymbol{\gamma}$.

Here we replaced κ' by γ'_{α}, which is possible since the two quantities are interchangeable through equation (6). The main reason to work with γ'_{α} is that in our data set, γ'_{α} is much noisier compared to the $\kappa'_{\rm g}$ due to the presence of the shape noise, therefore, converting γ'_{α} to κ'_{α} would be suboptimal to converting $\kappa'_{\rm g}$ to $\gamma'_{\alpha,{\rm g}}$. This choice depends somewhat on the specific data quality at hand. In addition, the term $\langle\gamma'^{N}_{\alpha,{\rm g}}\gamma'^{N}_{\alpha,{\rm g}}\rangle$ is introduced to account for the shot noise arising from the finite number of galaxies in the galaxy density field (see also Paper I). The term is calculated by randomizing the galaxy positions when calculating $\gamma'_{\alpha,{\rm g}}$. Finally, since $\langle\gamma'_{\alpha,{\rm g}}\gamma'_{\alpha}\rangle$ is noisy and can become close to zero, measuring directly the inverse of equation (21) results in a less stable and biased estimator. Therefore, we measure the inverse-bias, μ, throughout the analysis and only take the inverse at the very end to recover the galaxy bias b. This approach is similar to that used in A12. We show in Appendix A the results using b instead of μ as our main estimator.

The measurement from this method would depend on assumptions of the cosmological model in the construction of $\kappa'_{\rm g}$ and the calculation of f. Except for the literal linear dependence on $H_0\Omega_{\rm m}$, due to the ratio nature of the measurement, most other parameters tend to cancel out. Within the current constraints from *Planck*, the uncertainty in the cosmological parameters affect the measurements at the per cent level, which is well within the measurement errors (>10 per cent). All cosmological parameters used in the calculation of this work are consistent with the simulations described in Section 3.5.

2.5 Multiple source–lens samples

Whereas equations (20) and (21) describes how we measure galaxy bias for one source sample and one lens sample, in practice multiple different samples of lenses and the sources are involved. We define several source and lens samples, or 'bins', based on their photometric redshift (photo-z), with the lens samples labelled by 'i' and the source samples labelled by 'j'. We use the notation $\mu^{\alpha}_{\rm ij}$ to represent the inverse-bias measured with γ_{α} using the source bin j and lens bin i.

Our estimate of the galaxy bias in each lens redshift bin i is calculated by combining $\mu^{\alpha}_{\rm ij}$ estimates from the two components of

shear and all source redshift bins j. To combine these, we consider a least-square fit to the following model:

$$D_{\rm i} = \bar{\mu}_{\rm i} M, \tag{22}$$

where $D = \{\mu^{\alpha}_{\rm ij}\}$ is the data vector containing all the measurements $\mu^{\alpha}_{\rm ij}$ of galaxy bias in this lens bin i (including measurement from the two shear components and possibly multiple source bins), $\bar{\mu}_{\rm i}$ is the combined inverse-bias in each bin i we wish to fit for, and M is a 1D array of the same length as $D_{\rm i}$ with all elements being 1. Our final estimate of inverse-bias for redshift bin i, $\bar{\mu}_{\rm i}$, and its uncertainty $\sigma(\bar{\mu}_{\rm i})$ are

$$\bar{\mu}_{\rm i} = M_{\rm i}^{\rm T} C_{\rm i}^{-1} D_{\rm i} [M_{\rm i}^{\rm T} C_{\rm i}^{-1} M_{\rm i}]^{-1}, \tag{23}$$

$$\sigma(\bar{\mu}_{\rm i})^2 = (M_{\rm i}^{\rm T} C_{\rm i}^{-1} M_{\rm i})^{-1}, \tag{24}$$

where $C_{\rm i}^{-1}$ is the unbiased inverse covariant matrix (Hartlap, Simon & Schneider 2007) between all $\mu^{\alpha}_{\rm ij}$ measurements, estimated by Jack–Knife (JK) resampling:

$$C_{\rm i}^{-1} = \tau\ {\rm Cov}^{-1}[D_{\rm i}], \tag{25}$$

where $\tau = (N - \nu - 2)/(N - 1)$. N is the number of JK samples, and ν is the dimension of $C_{\rm i}$. Note that the matrix inversion of $C_{\rm i}$ becomes unstable when the measurements $\mu^{\alpha}_{\rm ij}$ are highly correlated. This is the case in the noiseless simulations. For the noisy simulations and data, however, it does not affect the results. The galaxy bias and its uncertainty is then

$$\bar{b}_{\rm i} = \frac{1}{\bar{\mu}_{\rm i}} \tag{26}$$

and

$$\sigma^2(\bar{b}_{\rm i}) = \frac{\sigma^2(\bar{\mu}_{\rm i})}{\bar{\mu}_{\rm i}^2}. \tag{27}$$

The uncertainty estimated through JK resampling does not account for cosmic variance and its coupling with the mask geometry. In Section 4.3, we further include the uncertainty from cosmic variance using simulations.

3 DATA AND SIMULATIONS

In this section we describe the data and simulation used in this work. We use the DES SV data collected using the Dark Energy Camera (Flaugher et al. 2015) from 2012 November to 2013 February and that have been processed through the data management pipeline described in Ngeow et al. (2006), Sevilla et al. (2011), Desai et al. (2012), and Mohr et al. (2012). Individual images are stacked, objects are detected and their photometric/morphological properties are measured using the software packages SCAMP (Bertin 2006), SWARP (Bertin et al. 2002), PSFEX (Bertin 2011), and SExtractor (Bertin & Arnouts 1996). The final product, the SVA1 Gold catalogue[7] is the foundation of all catalogues described below. We use a $\sim$116.2 deg^2 subset of the data in the South Pole Telescope-East (SPT-E) footprint, which is the largest contiguous region in the SV data set. This data set is also used in other DES weak lensing and large-scale structure analyses (Becker et al. 2015; Chang et al. 2015; The Dark Energy Survey Collaboration et al. 2015; Vikram et al. 2015; Crocce et al. 2016; Giannantonio et al. 2016).

[7] http://des.ncsa.illinois.edu/releases/sva1

3.1 Photo-z catalogue

The photo-z of each galaxy is estimated through the SKYNET code (Graff et al. 2014). SKYNET is a machine learning algorithm that has been extensively tested in Sánchez et al. (2014) and Bonnett et al. (2015) to perform well in controlled simulation tests. To test the robustness of our results, we also carry out our main analysis using two other photo-z codes which were tested in Sánchez et al. (2014) and Bonnett et al. (2015): BPZ (Benítez 2000) and TPZ (Carrasco Kind & Brunner 2013, 2014). We discuss in Section 4.5 the results from these different photo-z codes.

The photo-z codes output a PDF for each galaxy describing the probability of the galaxy being at redshift z. We first use the mean of the PDF, $z_{\rm mean}$ to separate the galaxies into redshift bins, and then use the full PDF to calculate equation (19). In Fig. 1, we show the normalized redshift distribution for each lens and source bin as defined below.

3.2 Galaxy catalogue

To generate the $\kappa_{\rm g}$ maps, we use the same 'benchmark' sample used in Giannantonio et al. (2016) and Crocce et al. (2016). This is a magnitude-limited galaxy sample at $18 < i < 22.5$ derived from the SVA1 Gold catalogue with additional cleaning with colour, region, and star–galaxy classification cuts (see Crocce et al. 2016, for full details of this sample). The final area is $\sim$116.2 deg^2 with an average galaxy number density of 5.6 arcmin^{-2}. Six redshift bins were used from $z_{\rm mean} = 0.0$ to 1.2 with $\Delta z_{\rm mean} = 0.2$. The magnitude-limited sample is constructed by using only the sky regions with limiting magnitude deeper than $i = 22.5$, where the limiting magnitude is estimated by modelling the survey depth as a function of magnitude and magnitude errors (Rykoff, Rozo & Keisler 2015). Various systematics tests on the benchmark has been performed in Crocce et al. (2016) and Leistedt et al. (2015).

3.3 Shear catalogue

Two shear catalogues are available for the DES SV data based on two independent shear measurement codes NGMIX (Sheldon 2014) and IM3SHAPE (Zuntz et al. 2013). Both catalogues have been tested rigorously in Jarvis et al. (2015) and have been shown to pass the requirements on the systematic uncertainties for the SV data. Our main analysis is based on NGMIX due to its higher effective number density of galaxies (5.7 compared to 3.7 arcmin^{-2} for IM3SHAPE). However, we check in Section 4.5.2 that both catalogues produce consistent results. We adopt the selection cuts recommended in Jarvis et al. (2015) for both catalogues. This galaxy sample is therefore consistent with the other DES SV measurements in e.g. Becker et al. (2015) and The Dark Energy Survey Collaboration et al. (2015). Similar to these DES SV papers, we perform all our measurements on a blinded catalogue (for details of the blinding procedure, see Jarvis et al. 2015), and only unblind when the analysis is finalized.

γ_1 and γ_2 maps are generated from the shear catalogues for five redshift bins between $z_{\rm mean} = 0.4$ and 1.4 with $\Delta z_{\rm mean} = 0.2$. Note part of the highest redshift bin lies outside of the recommended photo-z selection according to Bonnett et al. (2015) ($z_{\rm mean} = 0.3$–1.3). We discard the highest bin in the final analysis due to low signal-to-noise ratio (see Section 4.4), but for future work, however, it would be necessary to validate the entire photo-z range used.

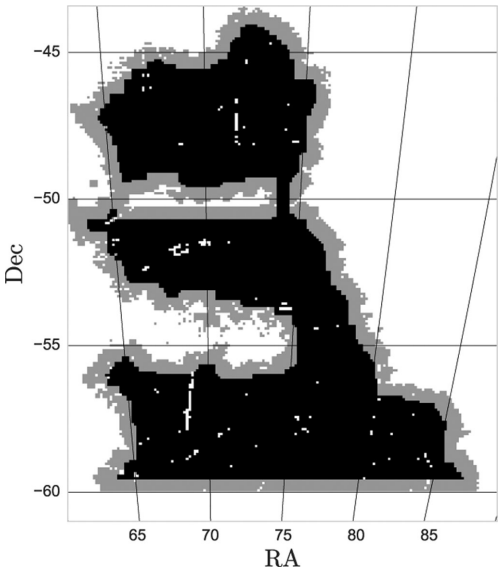

Figure 2. Mask used in this work. The black region shows where the galaxy bias is calculated (the *bias mask*). The black+grey map region is where all maps are made (the *map mask*).

3.4 Mask

Two masks are used in this work. First, we apply a common mask to all maps used in this work, we will refer this mask as the *'map mask'*. The mask is constructed by re-pixelating the $i > 22.5$ depth map into the coarser (flat) pixel grid of 5×5 arcmin^2 we use to construct all maps (see Section 4.1). The depth mask has a much higher resolution (Nside = 4096 HEALPIX map) than this grid, which means some pixels in the new grid will be partially masked in the original HEALPIX grid. We discard pixels in the new grid with more than half of the area masked in the HEALPIX grid. The remaining partially masked pixels causes effectively a ∼3 per cent increase in the total area. The partially masked pixels will be taken into account later when generating κ_g (we scale the mean number of galaxy per pixel by the appropriate pixel area). We also discard pixels without any source galaxies.

Pixels on the edges of our mask will be affected by the smoothing we apply to the maps. In addition, when performing the KS conversion, the mask can affect our results. We thus define a second *'bias mask'*, where we start from the *map mask* and further mask pixels that are closer than half a smoothing scale away from any masked pixels except for holes smaller than 1.5 pixels.[8] Both masks are shown in Fig. 2.

3.5 Simulations

In this work we use the same mock galaxy catalogue from the MICE simulations[9] (Crocce et al. 2015; Fosalba et al. 2015a,b) which is described in detail in Paper I. MICE adopts the ΛCDM cosmological parameters: $\Omega_m = 0.25$, $\sigma_8 = 0.8$, $n_s = 0.95$, $\Omega_b = 0.044$, $\Omega_\Lambda = 0.75$, and $h = 0.7$. The galaxy catalogue has been generated according to a halo occupation distribution (HOD) and a subhalo abundance matching (SHAM) prescription described in Carretero et al. (2015). The main tests were done with the region $0^\circ < \mathrm{RA} < 30^\circ$, $0^\circ < \mathrm{Dec.} < 30^\circ$, while we use a larger region ($0^\circ < \mathrm{RA} < 90^\circ$, $0^\circ < \mathrm{Dec.} < 30^\circ$) to estimate the effect from cosmic variance. We use the following properties for each galaxy in the catalogue – position on the sky (RA, Dec.), redshift (z), apparent magnitude in the i band, and weak lensing shear ($\boldsymbol{\gamma}$).

In addition, we incorporate shape noise and masking effects that are matched to the data. For shape noise, we draw randomly from the ellipticity distribution in the data and add linearly to the true shear in the mock catalogue to yield ellipticity measurements for all galaxies in the mock catalogue. We also make sure that the source galaxy number density is matched between simulation and data in each redshift bin. For the mask, we simply apply the same mask from the data to the simulations. Note that the unmasked simulation area is ∼8 times larger than the data, thus applying the mask increases the statistical uncertainty.

Finally, to investigate the effect of photo-z uncertainties, we add a Gaussian photo-z error to each MICE galaxy according to its true redshift. The standard deviation of the Gaussian uncertainty follows $\sigma(z) = 0.03(1 + z)$. This model for the photo-z error is simplistic, but since we use this set of photo-z simulations mainly to test our algorithm (the calculation of f in equation 19), we believe a simple model will serve its purpose.

We note that the larger patch of MICE simulation used in this work (∼30 × 30 deg^2) is of the order of what is expected for the first year of DES data (∼2000 deg^2 and ∼1 mag shallower). Thus, the simulation measurements shown in this work also serves as a rough forecast for our method applied on the first year of DES data.

4 ANALYSIS AND RESULTS

4.1 Procedure

Before we describe the analysis procedure, it is helpful to have a mental picture of a 3D cube in RA, Dec., and z. The z-dimension is illustrated in Fig. 1, with a coarse resolution of five redshift bins for both lenses and sources. Each lens and source sample is then collapsed into 2D maps in the RA/Dec. dimension. For each source bin, we can only constrain the galaxy bias using the lens bins at the foreground of this source bin. That is, for the highest source redshift bin there are five corresponding lens bins, and for the lowest source redshift bin there is only one lens bin. The analysis is carried out in the following steps.

First, we generate all the necessary maps for the measurement: γ_1, γ_2 maps for each source redshift bin j, and $\gamma'_{1,g}$, $\gamma'_{2,g}$, $\gamma'^N_{1,g}$, and $\gamma'^N_{2,g}$ maps for each lens bin i and source bin j. We generate random maps ($\gamma'^N_{1,g}$, $\gamma'^N_{2,g}$) for the calculation of $\langle \gamma'^N_{\alpha,g} \gamma'^N_{\alpha,g} \rangle$ in equation (21). All maps are generated using a sinusoidal projection at a reference RA of 71° and 5 arcmin^2 pixels on the projected plane. These maps are then smoothed by a 50 arcmin boxcar filter while the *map mask* is applied. The chosen pixel and smoothing scales are based on tests described in Paper I. For a given source bin, the value of each pixel in the γ_1 and γ_2 maps is simply the weighted mean of the shear measurements in the area of that pixel. The weights reflect the uncertainties in the shear measurements in the data, while we set all weights to 1 in the simulations. For a given lens bin, the pixel values of the $\gamma'_{1,g}$, $\gamma'_{2,g}$ maps are calculated through equation (14), where Σ' is the number of galaxies in that pixel, and $\bar{\Sigma}'$ is the mean

[8] The reason for not apodizing the small masks is that it would reduce significantly the region unmasked and thus the statistical power of our measurement. We have tested in simulations that the presence of these small holes does not affect our final measurements. We consider only pixels surviving the *bias mask* when estimating galaxy bias. Fig. 2 shows both masks used in this work.

[9] http://cosmohub.pic.es/

number of galaxies per pixel in that lens bin. For each combination of lens–source bins, we calculate μ_{ij}^{α} (equation 21) from the maps after applying the *bias mask*. We assume $\Delta\chi' \approx$ the width of the photo-z bin. f is calculated analytically through equation (19), where we use $\phi'(z) \propto p_l'(z)$, the estimated normalized redshift distribution from our photo-z code for each lens bin.

We combine all estimates for the same lens bin i through equations (23) and (24), where the covariance between the different measurements is estimated using 20 JK samples defined with a 'k-mean' algorithm (MacQueen 1967). The k-mean method splits a set of numbers (centre coordinate of pixels in our case) into several groups of numbers. The split is made so that the numbers in each group is closest to the mean of them. In our analysis it effectively divides our map into areas of nearly equal area, which we use as our JK regions. The different JK samples are slightly correlated due to the smoothing process. We estimate the effect of this smoothing on the error bars by comparing the JK error bars on the zero-lag autocorrelation of a random map (with the same size of the data) before and after applying the smoothing. For 20 JK samples, this is a ∼10 per cent effect on the error bars, which we will incorporate in the data measurements. We have also verified that the results are robust to the number of JK samples used. The above procedure is applied to the data and the simulations using the same analysis pipeline.

As hinted in Section 2.5, the error bars from JK resampling do not fully account for the uncertainties from cosmic variance. A more complete account for the uncertainty is to measure $\bar{\mu}_i$ for a large number of simulations that are closely matched to the data. We compare in Section 4.3 the resulting error estimation with and without including cosmic variance.

4.2 Linear fit

In the final step of our analysis, we fit a simple linear model of galaxy bias to the data. To do this, we take into account the full covariance between the $\bar{\mu}_i$ measurements in different redshift bins, which we estimate through simulations. In particular, we use a least-square approach similar to equation (23) and consider a linear model for the inverse galaxy bias in the following form:

$$D = \bar{\boldsymbol{\mu}} Z, \tag{28}$$

where $D = \{\bar{\mu}_i\}$ is now the vector containing the measured inverse galaxy bias in each lens redshift bin, $\bar{\boldsymbol{\mu}} = \{\bar{\mu}^0 \ \bar{\mu}^1\}$ is the vector composed of the two coefficients for the linear fit, and $Z = \begin{pmatrix} 1 \\ \bar{z}_i \end{pmatrix}$ is a 2D matrix with the first row being 1 and the second row containing the mean redshift of each lens bin. The least-square fit to this model and the errors on the fit then becomes

$$\bar{\boldsymbol{\mu}} = Z^{\mathrm{T}} C^{-1} D [Z^{\mathrm{T}} C^{-1} Z]^{-1}, \tag{29}$$

$$\sigma(\bar{\boldsymbol{\mu}})^2 = (Z^{\mathrm{T}} C^{-1} Z)^{-1}, \tag{30}$$

where

$$C^{-1} = \tau \, \mathrm{Cov}^{-1}[D]. \tag{31}$$

Here $\tau = (N - \nu - 2)/(N - 1)$ corrects for the bias in the inverse covariance matrix due to the finite number of simulations (Hartlap et al. 2007), where N is the number of simulation samples, and ν is the dimension of C. In Section 4.4, we only use the four lower redshift bin for the linear fit, as the highest redshift bin is unstable and noisy, so $\nu = 4$ in our final measurement for the data.

4.3 Simulation tests

Following the procedure outlined above, we present here the result of the redshift-dependent galaxy bias measurements from the MICE simulation. We start from an ideal set-up in the simulations that is very close to that used in Paper I and gradually degrade the simulations until they match our data. Below we list the series of steps we take:

(i) use the full area (∼900 deg^2) with the true $\boldsymbol{\gamma}$ maps;
(ii) repeat above with photo-z errors included;
(iii) repeat above with shape noise included;
(iv) repeat above with SV mask applied;
(v) repeat above with 12 different SV-like areas on the sky, and vary the shape noise 100 times for each.

Fig. 3 illustrates an example of how the $\gamma_{1,g}$ and γ_1 maps degrade over these tests. The left-hand column shows the $\gamma_{1,g}$ maps while the right-hand column shows the γ_1 maps. Note that the colour bars on the upper (lower) two maps in the right-hand panel are two (four) times higher compared to the left-hand column. This is to accommodate for the large change in scales on the right arising from shape noise in the γ_1 maps. The first row corresponds to (i) above, and we can visually see the correspondence of some structures between the two maps. Note that the $\gamma_{1,g}$ map only contributes to part of the γ_1 map, which is the reason that we do not expect even the true $\gamma_{1,g}$ and γ_1 maps to agree perfectly. The second row shows the map with photo-z errors included, corresponding to the step (ii). We find that the real structures in the maps are smoothed by the photo-z uncertainties, lowering the amplitude of the map. The smoothing from the photo-z is more visible in the $\gamma_{1,g}$ map, since the γ_1 map probes an integrated effect and is less affected by photo-z errors. The third row shows what happens when shape noise is included, which corresponds to the step (iii) above. We find the structures in the γ_1 map becomes barely visible in the presence of noise, with the amplitude much higher than the noiseless case as expected. The bottom row corresponds to the step (iv) above, where the SV mask is applied to both maps. For the γ_1 map this is merely a decrease in the area. But for the $\gamma_{1,g}$ map, this also affects the conversion from κ_g to $\boldsymbol{\gamma}_g$, causing edge effects in the $\gamma_{1,g}$ map which are visible in the bottom left-hand map in Fig. 3. Step (v) is achieved by moving the mask around and drawing different random realizations of shape noise for the source galaxies.

With all maps generated, we then calculate the redshift-dependent galaxy bias following equations (23) and (24) for each of the steps from (i) to (v). In Fig. 4 we show the result for the different stages, overlaid with the bias from the 2PCF measurement described in Paper I. In step (i), our measurements recover the 2PCF estimates, confirming the results in Paper I, that we can indeed measure the redshift-dependent bias using this method under appropriate settings. Our error bars are smaller than that in Paper I, which is due to the fact that we have combined measurements from several source bins, and that we estimate inverse-bias instead of bias directly. Since the only difference between this test and the test in Paper I is the inclusion of the KS conversion, we have also shown that the KS conversion in the noiseless case does not introduce significant problems in our measurements. The error bars on the highest redshift bin are large due to the small number of source and lens galaxies. In step (ii), we introduce photo-z errors. We find that the photo-z errors do not affect our measurements within the measurement uncertainties. In step (iii), the error bars increase due to the presence of shape noise. In step (iv), we apply the SV mask, making the result much noisier due to the smaller area. We repeat

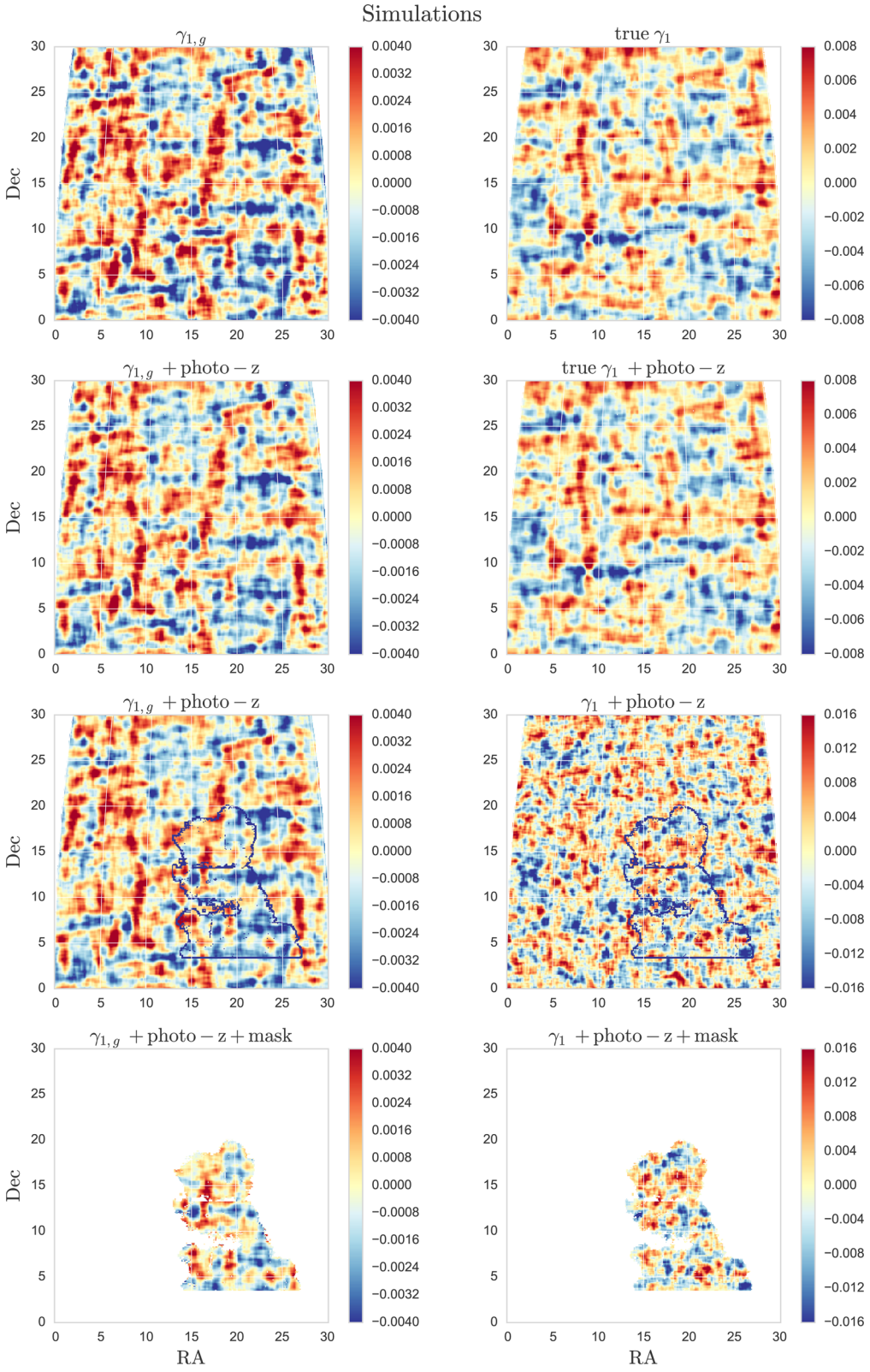

Figure 3. Example of simulation maps used in this work. The left-hand column shows $\gamma_{1,\mathrm{g}}$ maps and the right-hand column shows γ_1 maps. This $\gamma_{1,\mathrm{g}}$ maps are generated from the source redshift bin z (or z_{mean}) = 1.0–1.2 and the lens redshift bin z (or z_{mean}) = 0.4–0.6. The γ_1 maps are generated from the source redshift bin z (or z_{mean}) = 1.0–1.2. The galaxy bias for the lens galaxies can be measured by cross-correlating the left- and the right-hand column. From top to bottom illustrates the different stages of the degradation of the simulations to match the data. The first row shows the $\gamma_{1,\mathrm{g}}$ map against the true γ_1 map for the full 30 × 30 deg^2 area. The second row shows the same maps with photo-z errors included, slightly smearing out the structures in both maps. The third row shows the same $\gamma_{1,\mathrm{g}}$ map as before against the γ_1 that contains shape noise, making the amplitude higher. Finally, the bottom row shows both maps with the SV mask applied, which is also marked in the third row for reference. Note that the colour scales on the γ_1 maps is two (four) times higher in the upper (lower) two panels than that of the $\gamma_{1,\mathrm{g}}$ maps.

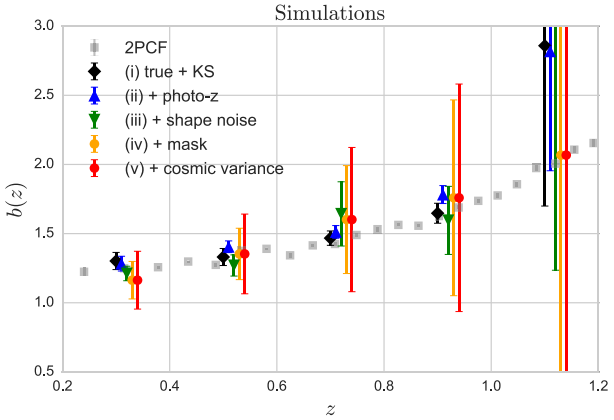

Figure 4. Redshift-dependent galaxy bias measured from simulations with different levels of degradation from the ideal scenario tested in Paper I. The grey line shows the bias from the 2PCF measurement, which we take as 'truth'. The black, blue, green, orange, and red points corresponding to the steps (i), (ii), (iii), (iv), and (v) in Section 4.3, respectively. The error bars in (i), (ii), and (iii) correspond to the JK error bars (equation 24). The error bars for (iv) is the mean JK error bars for 1200 simulations while the error bars for (v) is the standard deviation of the measurements of 1200 simulations.

this step on 12 different SV-like areas in a larger (30×90 deg^2) simulation area and vary the shape noise realization 100 times for each area. The orange points in Fig. 4 shows the average measurement and JK error bars of these 1200 simulations. We find that albeit the large uncertainties, our method indeed gives an unbiased estimation of the redshift dependent of bias which is consistent with the 2PCF estimations. In step (v), we account for the additional uncertainty in our measurements due to cosmic variance. The red points are the same as the orange points, except that the error bars are estimated from the standard deviation of the 1200 measurements in the simulations. We find that the contribution to the uncertainties from cosmic variance can be important especially at low redshift.

With the series of simulation tests above, we have shown that our measurement method itself is well grounded, but the presence of measurement effects and noise can introduces large uncertainties in the results. In the next section, we continue with the same measurement on DES SV data and will use the full simulation covariance derived in this section for the final fitting process. We believe the simulation covariance matrix captures the dominant sources of uncertainties in the problem.

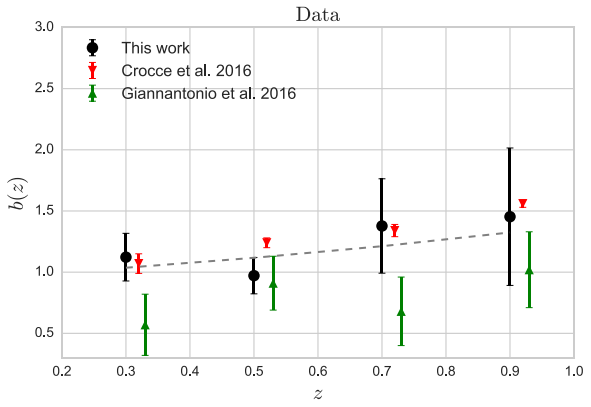

Figure 6. Redshift-dependent bias measured from the DES SV data. The black data points show the result from this work. The red and green points show the measurements on the same galaxy sample with different methods. The grey dashed line is the best fit to the black data points.

4.4 Redshift-dependent galaxy bias of DES SV data

We now continue to measure redshift-dependent galaxy bias with the DES SV data using the same procedure as in the simulations. Fig. 5 shows some examples of the maps. The rightmost panel shows the γ_1 map at redshift bin $z_{\rm mean} = 1.0$–1.2, while the rest of the maps are the $\gamma_{1,g}$ maps at different redshift bin evaluated for this γ_1 map. We see the effect of the lensing kernel clearly: the leftmost panel is at the peak of the lensing kernel, giving it a higher weight compared to the other lens bins. We also see correlations between $\gamma_{1,g}$ maps at different redshift bins. This is a result of the photo-z contamination.

In Fig. 6 we show the galaxy bias measurement for our magnitude-limited galaxy sample from DES SV together with two other independent measurements with the same galaxy sample (discussed in Section 5). We have excluded the highest redshift bin since with only a small number of source galaxies, the constraining power from lensing in that bin is very weak. The black data points show the measurement and uncertainty estimated from this work, with a best-fitting linear model of $\mu(z) = 1.07^{\pm 0.24} - 0.35^{\pm 0.42} z$. The error bars between the redshift bins are correlated, and have been taken into account during the fit. Table 2 summarizes the results.

As discussed earlier, our method becomes much less constraining going to higher redshift, as the source galaxies become sparse. This is manifested in the increasingly large error bars going to high redshifts. Here we only performed a simple linear fit to the data

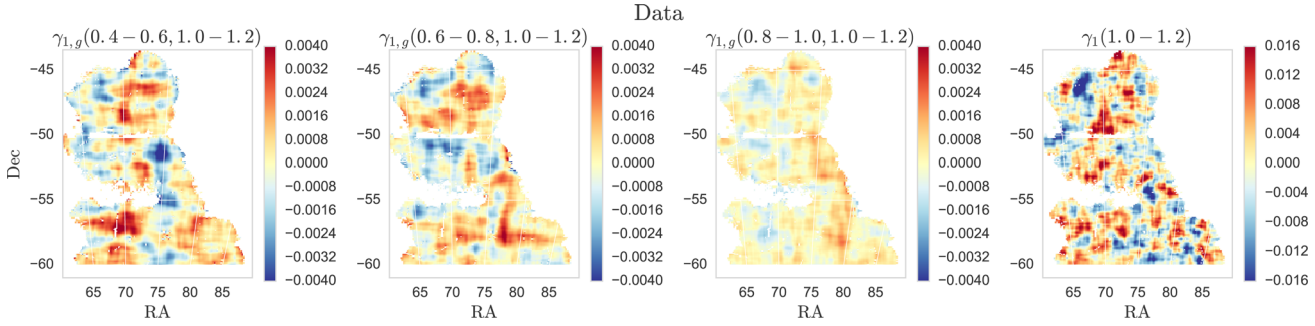

Figure 5. Example of maps from DES SV data. The rightmost panel shows the γ_1 map generated from the source redshift bin $z_{\rm mean} = 1.0$–1.2, while the other panels show the $\gamma_{1,g}$ maps generated for the source redshift bin $z_{\rm mean} = 1.0$–1.2 and for different lens redshifts (left: $z_{\rm mean} = 0.4$–0.6; middle: $z_{\rm mean} = 0.6$–0.8; right: $z_{\rm mean} = 0.8$–1.0). The title in each panel for $\gamma_{1,g}$ indicate the lens and source redshift, while the title for γ_1 indicates the source redshift. Note that the colour bars are in different ranges, but are matched to the simulation plot in Fig. 3. In addition, the leftmost and the rightmost panels correspond to the bottom row of that figure.

Table 2. Bias measurement and 1σ error bars from DES SV using the method tested in this work, with all possible lens–source combinations. We also compare here our main measurements with that using alternative shear and photo-z catalogues. Finally, we compare our results with other measurement methods carried out on the same data set. The Crocce et al. (2016) estimates are from table 3 in that paper, while the Giannantonio et al. (2016) estimates are from table 2 in that paper.

	Lens redshift ($z_{\rm mean}$)			
	0.2–0.4	0.4–0.6	0.6–0.8	0.8–1.0
This work (NGMIX+SKYNET)	$\mathbf{1.12 \pm 0.19}$	$\mathbf{0.97 \pm 0.15}$	$\mathbf{1.38 \pm 0.39}$	$\mathbf{1.45 \pm 0.56}$
This work (IM3SHAPE+SKYNET)	1.21 ± 0.25	1.12 ± 0.24	0.90 ± 0.19	0.91 ± 0.28
This work (NGMIX+TPZ)	1.23 ± 0.23	1.07 ± 0.18	1.39 ± 0.40	1.29 ± 0.44
This work (NGMIX+BPZ)	0.84 ± 0.11	1.00 ± 0.16	1.13 ± 0.26	0.95 ± 0.24
Crocce et al. (2016)	1.07 ± 0.08	1.24 ± 0.04	1.34 ± 0.05	1.56 ± 0.03
Giannantonio et al. (2016)	0.57 ± 0.25	0.91 ± 0.22	0.68 ± 0.28	1.02 ± 0.31

given the large uncertainties in our measurements. In the future, one could extend to explore more physically motivated galaxy bias models (Matarrese et al. 1997; Clerkin et al. 2015).

Compared with A12, our data set is approximately ∼105 times larger, but with a (source) galaxy number density ∼11.6 times lower. This yields roughly ∼3 times lower statistical uncertainty in our measurement. Our sample occupies a volume slightly larger than the $0 < z < 1$ sample in A12. Note, however, that due to photo-z uncertainties and the high shape noise per unit area, we expect a slightly higher level of systematic uncertainty in our measurement. Since in A12, the emphasis was not on measuring linear bias, one should take caution in comparing directly our measurement with A12. But we note that the large uncertainties at $z > 0.6$ and the weak constraints on the redshift evolution in the galaxy bias is also seen in A12. To give competitive constraints on the redshift evolution, higher redshift source planes would be needed.

4.5 Other systematics test

In Section 4.3, we have checked for various forms of systematic effects coming from the KS conversion, finite area, complicated mask geometry, and photo-z errors. Here we perform three additional tests. First, we check that the cross-correlation between the B-mode shear $\boldsymbol{\gamma}_{\rm B}$ and $\boldsymbol{\gamma}_{\rm g}$ is small. Next, we check that using the second DES shear pipeline, IM3SHAPE gives consistent answers with that from NGMIX. Finally, we check that using two other photo-z codes also give consistent results. These three tests show that there are no significant systematic errors in our measurements.

4.5.1 B-mode test

Lensing B-mode refers to the divergent-free piece of the lensing field, which is zero in an ideal, noiseless scenario. As a result, B-mode is one of the measures for systematic effects in the data. In Jarvis et al. (2015), a large suite of tests have been carried out to ensure that the shear measurements have lower level of systematic uncertainties compared to the statistical uncertainties. Nevertheless, here we test in specific the B-mode statistics relevant to our measurements.

We construct a $\boldsymbol{\gamma}_{\rm B}$ field by rotating the shear measurements in our data by 45°, giving

$$\boldsymbol{\gamma}_{\rm B} = \gamma_{\rm B,1} + {\rm i}\gamma_{B,2} = -\gamma_2 + {\rm i}\gamma_1. \quad (32)$$

Substituting $\boldsymbol{\gamma}_{\rm B}$ into $\boldsymbol{\gamma}$ in our galaxy bias calculation (equation 21) gives an analogous measurement to b, which we will refer to as $b_{\rm B}$. Since we expect $\boldsymbol{\gamma}_{\rm B}$ not to correlate well with $\boldsymbol{\gamma}_{\rm g}$, $1/b_{\rm B}$ would ideally go to zero. In Fig. 7, we show all the $b_{\rm B}$ measurements using both shear component and all lens–source combinations. We see that all the data points are consistent with zero at the 1–2σ level, assuring that the B-modes in the shear measurements are mostly consistent with noise. We also show the weighted mean of all the data points and the corresponding B-mode measurements from one of the simulation used in Section 4.3 (iv). We see that the level and scatter in the data are compatible with that in the simulations.

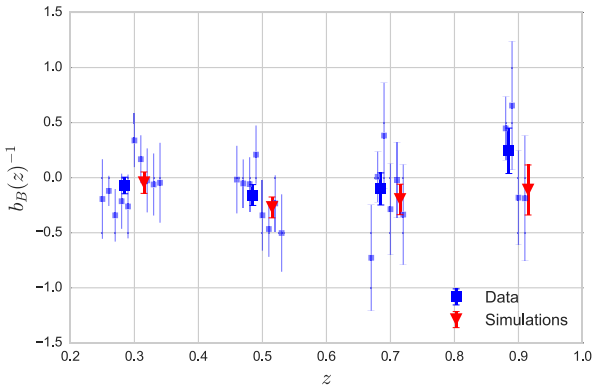

Figure 7. All $1/b_{\rm B}(z)$ measurements from the B-mode shear and the same $\boldsymbol{\gamma}_{\rm g}$ in our main analysis. Each small blue data point represents a measurement from a combination of lens redshift, source redshift, and shear component. Note that the low-redshift bins contain more data points, as there are more source galaxies that can be used for the measurement. The large blue points are the weighted mean of all measurements at the same redshift bin from the DES SV data, while the red points are that from simulations that are well matched to data.

4.5.2 IM3SHAPE test

As described in Section 3.3, two independent shear catalogues from DES SV were constructed. Here, we perform the same measurement in our main analysis using the IM3SHAPE catalogue. The IM3SHAPE catalogue contains less galaxies, thus the measurements are slightly noisier. The resulting redshift-dependent galaxy measurements are shown in Table 2 and are overall slightly higher than the NGMIX measurements, and there is almost no constraining power on the evolution. The best-fitting linear bias model is $\mu(z) = 0.64^{\pm 0.28} + 0.56^{\pm 0.52} z$, which is consistent with the NGMIX measurements at the 1σ level. The B-modes (not shown here) are similar to Fig. 7.

4.5.3 Photo-z test

As mentioned in Section 3.1, several photo-z catalogues were generated for the DES SV data set and shown in Bonnett et al. (2015) to

meet the required precision and accuracy for the SV data. All above analyses were carried out with the SKYNET photo-z catalogue. Here we perform the exact same analysis using the other two catalogues: BPZ and TPZ. In specific, to be consistent with the other DES SV analyses (Becker et al. 2015; The Dark Energy Survey Collaboration et al. 2015), we keep the tomographic bins unchanged (binned by SKYNET mean redshift), but use the $p(z)$ from the different photo-z codes to calculate f. The lensing or galaxy maps themselves remain unchanged.

Table 2 lists the results from the different photo-z catalogues. Since SKYNET and TPZ are both machine learning codes and respond to systematic effects in a similar fashion, while BPZ is a template fitting code, we can thus view the difference between the results from BPZ and the others as a rough measure of the potential systematic uncertainty in our photo-z algorithm (see also discussion in Bonnett et al. 2015), which is shown here to be within the 1σ error bars.

5 COMPARISON WITH OTHER MEASUREMENTS

The redshift-dependent galaxy bias has been measured on the same data set using other approaches. Here we compare our result with two other measurements – galaxy clustering (Crocce et al. 2016, hereafter C16) and cross-correlation of galaxies and CMB lensing (Giannantonio et al. 2016, hereafter G16). We note that both these analyses assumed the most recent *Planck* cosmological parameters (Planck Collaboration XVI 2014), which is slightly different from our assumptions (see Section 3.5). But since our measurement depends very weakly on the assumption of cosmological parameters (as discussed in Section 2.4), the stronger cosmology dependencies come from the cosmological parameters assumed in C16 and G16, which are known well within our measurement uncertainties. We also note that the results we quote in Table 2 are based on the photo-z code TPZ, which means our redshift binning is not completely identical to theirs.

5.1 Bias measurement from galaxy clustering

In C16, galaxy bias was estimated through the ratio between the projected galaxy angular correlation function (2PCF) in a given redshift bin and an analytical dark matter angular correlation function predicted at the same redshift. The latter includes both linear and non-linear dark matter clustering derived from CAMB (Lewis, Challinor & Lasenby 2000) assuming a set of cosmological parameters. In C16, a flat ΛCDM+ν cosmological model based on *Planck* 2013+*Wilkinson Microwave Anisotropy Probe* (*WMAP*) polarization+Atacama Cosmology Telescope (ACT)/South Pole Telescope (SPT)+baryon acoustic oscillations (BAO) was used. The results in C16 as listed in Table 2 were shown to be consistent with the independent measurement from the Canada–France–Hawaii Telescope Legacy Survey (CFHTLS; Coupon et al. 2012).

Compared to C16, our work aims to measure directly the local galaxy bias (equation 1) instead of the galaxy bias defined through the 2PCF (equation 2). Although the two measurements agree in the linear regime where this work is based on, comparing the measurements on smaller scales will provide further insight to these galaxy bias models. Our method is less sensitive to assumptions of cosmological parameters compared to the 2PCF method. In particular, it does not depend strongly on σ_8, which breaks the degeneracy between σ_8 and the measured galaxy bias b in other measurement methods. Finally, since our measurement is a cross-correlation method (compared to C16, an autocorrelation method), it suffers less from systematic effects that only contaminate either the lens or the source sample. On the other hand, however, lensing measurements are intrinsically noisy and the conversion between shear and convergence is not well behaved in the presence of noise and complicated masking. In addition, we only considered a one-point estimate (zero-lag correlation), which contains less information compared to the full 2PCF functions. All these effects result in much less constraining power in our measurements.

As shown in Fig. 6 and listed in Table 2, our measurements and C16 agree very well except for the redshift bin $z = 0.4$–0.6 (slightly more than 1σ discrepancy). We note, however, both C16 and our work may not have included the complete allocation of systematic errors (especially those coming from the photo-z uncertainties), which could introduce some of the discrepancies.

5.2 Bias measurement from cross-correlation of galaxies and CMB lensing

In G16, galaxy bias is estimated by the ratio between the galaxy–CMB convergence cross-correlation and an analytical prediction of the dark matter–CMB convergence cross-correlation, both calculated through the 2PCF (and also in harmonic space through the power spectrum). Since the lensing efficiency kernel of the CMB is very broad and the CMB lensing maps are typically noisy, this method has less constraining power than C16. However, by using an independent external data, the CMB lensing maps from the SPT and the *Planck* satellite, this measurement serves as a good cross-check for possible systematic effects in the DES data.

In calculating the theoretical dark matter–CMB convergence cross-correlation, G16 also assumed a fixed cosmology and derived all predictions using CAMB. The σ_8–b degeneracy is thus also present in their analysis. We note, however, that one could apply our method to the CMB lensing data and avoid this dependency. In our framework, the CMB lensing plane will serve as an additional source plane at redshift $\sim$1100. We defer this option to future work.

The results from G16 are shown in Fig. 6 and listed in Table 2. These results come from the ratio between the measured and the predicted power spectrum, which suffers less from non-linear effects compared to the measurement in real space (2PCF). We find that G16 are systematically lower than our measurement at the 1–2σ level for all redshift bins. G16 also have more constraining power at high redshift compared to our results, as expected. Possible reasons for the discrepancy at low redshift include systematic errors (in e.g. the photo-z estimation) that are not included in either C16, G16, or this work. In addition, the redshift bins are significantly covariant, making the overall discrepancy less significant. Finally, the scales used in the three studies are slightly different. We refer the readers to G16 for more discussion of this discrepancy.

6 CONCLUSION

In this paper, we present a measurement of redshift-dependent bias using a novel technique of cross-correlating the weak lensing shear maps and the galaxy density maps. The method serves as an alternative measurement to the more conventional techniques such as two-point galaxy clustering, and is relatively insensitive to the assumed cosmological parameters. The method was first developed in A12 and later tested more rigorously with simulations in a companion paper (Paper I). Here we extend the method and apply it on wide-field photometric galaxy survey data for the first time. We measure the galaxy bias for a magnitude-limited galaxy sample in the DES SV data.

Following from Paper I, we carry out a series of simulation tests which incorporate step-by-step realistic effects in our data including shape noise, photo-z errors, and masking. In each step, we investigate the errors introduced in our estimation of galaxy bias. We find that shape noise and cosmic variance are the main sources of uncertainties, while the photo-z affects the measurements in a predictable way if the characteristics of the photo-z uncertainties are well understood. As the measurement itself is very noisy, simulation tests where we know the 'truth' provide a good anchor for building the analysis pipeline.

In our main analysis, we measure the galaxy bias with an $18 < i < 22.5$ magnitude-limited galaxy sample in four tomographic redshift bins to be 1.12 ± 0.19 ($z = 0.2$–0.4), 0.97 ± 0.15 ($z = 0.4$–0.6), 1.38 ± 0.39 ($z = 0.6$–0.8), and 1.45 ± 0.56 ($z = 0.8$–1.0). Measurements from higher redshifts are too noisy to be constraining. The best-fitting linear model gives $b^{-1}(z) = \mu(z) = 1.07^{\pm 0.24} - 0.35^{\pm 0.42} z$. The results are consistent between different shear and photo-z catalogues.

The galaxy bias of this same galaxy sample has also been measured with two other techniques described in C16 and G16. The three measurements agree at the 1–2σ level at all four redshift bins, though the results from G16 are systematically lower than our measurements. We note that our method is more constraining at low-redshift regions where there are more source galaxies behind the lens galaxies. As pointed out in A12, to constrain the evolution of galaxy bias, our current data set may not be optimal. A more efficient configuration would be combining a wide, shallow data set with a narrow, deep field. We plan on exploring these possibilities in the future. The main uncertainty in this work comes from the combined effect of masking, shape noise, and cosmic variance. However, as we demonstrated with simulations, moving to the larger sky coverage of the first and second year of DES data would reduce this effect significantly.

We have demonstrated the feasibility and validity of our method for measuring galaxy bias on a wide-field photometric data set. Looking forward to the first and second year of DES data ($\sim$2000 deg^2 and $\sim$1 mag shallower), we expect to explore a variety of other topics using this method with the increased statistical power. For example, the same measurement could be carried out on different subsamples of lens galaxies (in magnitude, colour, galaxy type, etc.) and gain insight into the different clustering properties for different galaxy populations. Also, one can extend the measurement into the non-linear regime and measure the scale dependencies of the galaxy bias. Finally, it would be interesting to compare the measurement from the 2PCF method and our method (which is a measure of local bias) on different scales to further understand the connections between the two galaxy bias models.

ACKNOWLEDGEMENTS

We thank Marc Manera, Donnacha Kirk, Andrina Nicola, Sebastian Seehars for useful discussion and feedback. CC, AA, AR, and TK are supported by the Swiss National Science Foundation grants 200021-149442 and 200021-143906. AP was supported by beca FI and 2009-SGR-1398 from Generalitat de Catalunya and project AYA2012-39620 from MICINN. JZ and SB acknowledge support from the European Research Council in the form of a Starting Grant with number 240672.

We are grateful for the extraordinary contributions of our CTIO colleagues and the DECam Construction, Commissioning and Science Verification teams in achieving the excellent instrument and telescope conditions that have made this work possible. The success of this project also relies critically on the expertise and dedication of the DES Data Management group.

Funding for the DES Projects has been provided by the US Department of Energy, the US National Science Foundation, the Ministry of Science and Education of Spain, the Science and Technology Facilities Council of the United Kingdom, the Higher Education Funding Council for England, the National Center for Supercomputing Applications at the University of Illinois at Urbana-Champaign, the Kavli Institute of Cosmological Physics at the University of Chicago, the Center for Cosmology and Astro-Particle Physics at the Ohio State University, the Mitchell Institute for Fundamental Physics and Astronomy at Texas A&M University, Financiadora de Estudos e Projetos, Fundação Carlos Chagas Filho de Amparo à Pesquisa do Estado do Rio de Janeiro, Conselho Nacional de Desenvolvimento Científico e Tecnológico and the Ministério da Ciência, Tecnologia e Inovação, the Deutsche Forschungsgemeinschaft and the Collaborating Institutions in the Dark Energy Survey.

The Collaborating Institutions are Argonne National Laboratory, the University of California at Santa Cruz, the University of Cambridge, Centro de Investigaciones Energéticas, Medioambientales y Tecnológicas-Madrid, the University of Chicago, University College London, the DES-Brazil Consortium, the University of Edinburgh, the Eidgenössische Technische Hochschule (ETH) Zürich, Fermi National Accelerator Laboratory, the University of Illinois at Urbana-Champaign, the Institut de Ciències de l'Espai (IEEC/CSIC), the Institut de Física d'Altes Energies, Lawrence Berkeley National Laboratory, the Ludwig-Maximilians Universität München and the associated Excellence Cluster Universe, the University of Michigan, the National Optical Astronomy Observatory, the University of Nottingham, The Ohio State University, the University of Pennsylvania, the University of Portsmouth, SLAC National Accelerator Laboratory, Stanford University, the University of Sussex, and Texas A&M University.

The DES data management system is supported by the National Science Foundation under Grant Number AST-1138766. The DES participants from Spanish institutions are partially supported by MINECO under grants AYA2012-39559, ESP2013-48274, FPA2013-47986, and Centro de Excelencia Severo Ochoa SEV-2012-0234. Research leading to these results has received funding from the European Research Council under the European Union's Seventh Framework Programme (FP7/2007-2013) including ERC grant agreements 240672, 291329, and 306478.

REFERENCES

Amara A. et al., 2012, MNRAS, 424, 553 (A12)
Bartelmann M., Schneider P., 2001, Phys. Rep., 340, 291
Becker M. R. et al., 2015, preprint (arXiv:1507.05598)
Benítez N., 2000, ApJ, 536, 571
Bertin E., 2006, in Gabriel C., Arviset C., Ponz D., Enrique S., eds, ASP Conf. Ser. Vol. 351, Astronomical Data Analysis Software and Systems XV. Astron. Soc. Pac., San Francisco, p. 112
Bertin E., 2011, in Evans I. N., Accomazzi A., Mink D. J., Rots A. H., eds, ASP Conf. Ser. Vol. 442, Astronomical Data Analysis Software and Systems XX. Astron. Soc. Pac., San Francisco, p. 435
Bertin E., Arnouts S., 1996, A&AS, 117, 393
Bertin E., Mellier Y., Radovich M., Missonnier G., Didelon P., Morin B., 2002, in Bohlender D. A., Durand D., Handley T. H., eds, ASP Conf. Ser. Vol. 281, Astronomical Data Analysis Software and Systems XI. Astron. Soc. Pac., San Francisco, p. 228
Blake C., Collister A., Lahav O., 2008, MNRAS, 385, 1257
Blanton M., 2000, ApJ, 544, 63
Bonnett C. et al., 2015, preprint (arXiv:1507.05909)

Carrasco Kind M., Brunner R. J., 2013, MNRAS, 432, 1483
Carrasco Kind M., Brunner R. J., 2014, MNRAS, 442, 3380
Carretero J., Castander F. J., Gaztañaga E., Crocce M., Fosalba P., 2015, MNRAS, 447, 646
Chang C. et al., 2015, Phys. Rev. Lett., 115, 051301
Clerkin L., Kirk D., Lahav O., Abdalla F. B., Gaztañaga E., 2015, MNRAS, 448, 1389
Coupon J. et al., 2012, A&A, 542, A5
Cresswell J. G., Percival W. J., 2009, MNRAS, 392, 682
Crocce M., Castander F. J., Gaztañaga E., Fosalba P., Carretero J., 2015, MNRAS, 453, 1513
Crocce M. et al., 2016, MNRAS, 455, 4301 (C16)
Desai S. et al., 2012, ApJ, 757, 83
Eriksen M., Gaztanaga E., 2015, preprint (arXiv:1508.00035)
Flaugher B. et al., 2015, AJ, 150, 150
Fosalba P., Gaztañaga E., Castander F. J., Crocce M., 2015a, MNRAS, 447, 1319
Fosalba P., Crocce M., Gaztañaga E., Castander F. J., 2015b, MNRAS, 448, 2987
Giannantonio T. et al., 2016, MNRAS, 456, 3213 (G16)
Graff P., Feroz F., Hobson M. P., Lasenby A., 2014, MNRAS, 441, 1741
Hartlap J., Simon P., Schneider P., 2007, A&A, 464, 399
Jarvis M. et al., 2015, MNRAS, submitted (arXiv:1507.05603)
Jullo E. et al., 2012, ApJ, 750, 37
Kaiser N., 1984, ApJ, 284, L9
Kaiser N., Squires G., 1993, ApJ, 404, 441
Leistedt B. et al., 2015, preprint (arXiv:1507.05647)
Lewis A., Challinor A., Lasenby A., 2000, ApJ, 538, 473
MacQueen J., 1967, in Le Cam L. M., Neyman J., eds, Proceedings of the Fifth Berkeley Symposium on Mathematical Statistics and Probability, Vol. 1, Statistics. Univ. California Press, Berkeley, CA, p. 281 (http://projecteuclid.org/euclid.bsmsp/1200512992)
Mandelbaum R., Slosar A., Baldauf T., Seljak U., Hirata C. M., Nakajima R., Reyes R., Smith R. E., 2013, MNRAS, 432, 1544
Manera M., Gaztañaga E., 2011, MNRAS, 415, 383
Matarrese S., Coles P., Lucchin F., Moscardini L., 1997, MNRAS, 286, 115
Mohr J. J. et al., 2012, Proc. SPIE, 8451, 84510D
Ngeow C. et al., 2006, Proc. SPIE, 6270, 627023
Planck Collaboration XVI, 2014, A&A, 571, A16
Pujol A. et al., 2016, preprint (arXiv:1601.00160) (Paper I)
Rykoff E. S., Rozo E., Keisler R., 2015, AJ, submitted (arXiv:1509.00870)
Sánchez C. et al., 2014, MNRAS, 445, 1482
Schneider P., 1998, ApJ, 498, 43
Sevilla I. et al., 2011, preprint (arXiv:1109.6741)
Sheldon E. S., 2014, MNRAS, 444, L25
Simon P., Hetterscheidt M., Schirmer M., Erben T., Schneider P., Wolf C., Meisenheimer K., 2007, A&A, 461, 861
Simon P., Hetterscheidt M., Wolf C., Meisenheimer K., Hildebrandt H., Schneider P., Schirmer M., Erben T., 2009, MNRAS, 398, 807
Swanson M. E. C., Tegmark M., Blanton M., Zehavi I., 2008, MNRAS, 385, 1635
The Dark Energy Survey Collaboration et al., 2015, preprint (arXiv:1507.05552)
Vikram V. et al., 2015, Phys. Rev. D, 92, 022006
Wild V. et al., 2005, MNRAS, 356, 247
Zehavi I. et al., 2011, ApJ, 736, 59
Zuntz J., Kacprzak T., Voigt L., Hirsch M., Rowe B., Bridle S., 2013, MNRAS, 434, 1604

APPENDIX A: CHOICE OF ESTIMATOR

In our main analysis, we use the inverse-galaxy bias $\mu = 1/b$ as our main estimator instead of estimating galaxy bias directly. In this appendix we show the effect of using b as the estimator. The origin of the difference comes from the fact that when combining the multiple measurements in the same lens bin, we use the least-square formalism equation (23), which relies on the covariance matrix C_i estimated through JK resampling. This covariance matrix can become ill-behaved depending on the estimator used. In our case, the denominator of b (the inverse of equation 21) can become close to zero, which makes the inversion of the covariance matrix unstable. We find that this introduces a bias in our final result, which will need to be calibrated.

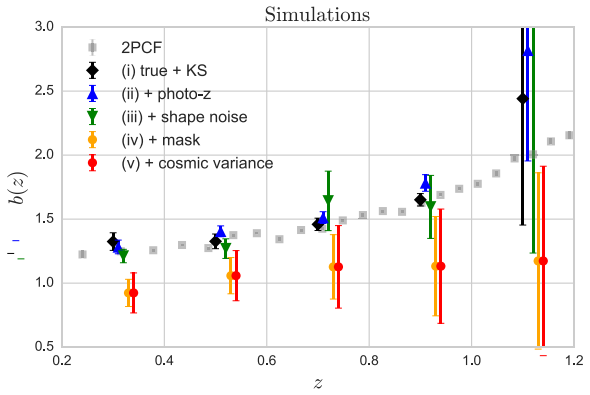

Figure A1. Same as Fig. 4, but using b as the estimator.

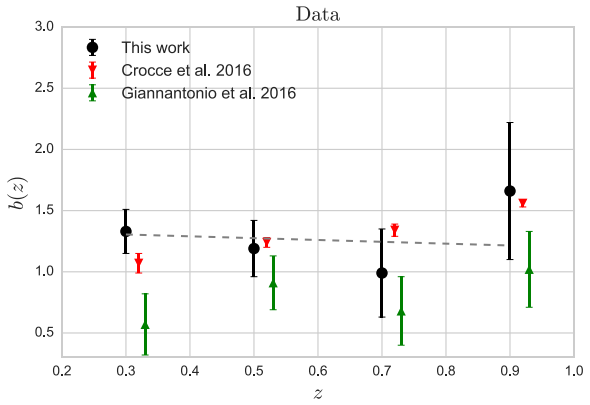

Figure A2. Same as Fig. 6, but using b as the estimator.

In Fig. A1 we show the equivalent of Fig. 4 using b as an estimator instead of μ. As the distribution of b estimated through the simulations have large outliers, we exclude simulations with bias estimates below 0 and above 5. We find that the main difference between Fig. 4 and Fig. A1 is in the orange and red points, where all the observational effects are included. For the less noisy scenarios (i), (ii), and (iii), the change is very minor. This is because the effect is more manifested when the measurements are noisy. The final (red) points in Fig. A1 is biased from the 'truth' by Δb due to the matrix inversion discussed above.

Once we calibrate Δb from these simulations and apply it to the data measurements, we have Fig. A2, which is the equivalent of Fig. 6 but using b as an estimator instead of μ. We find that after taking into account the bias derived from Fig. 4, the final measurements from the data is still consistent with our main analysis in Fig. 6. Nevertheless, as using b relies heavily of the quality of the simulations and the outlier rejection described above is not entirely objective, we choose to use the estimator μ instead.

[1]*Department of Physics, ETH Zurich, Wolfgang-Pauli-Strasse 16, CH-8093 Zurich, Switzerland*
[2]*Institut de Ciències de l'Espai, IEEC-CSIC, Campus UAB, Facultat de Ciències, Torre C5 par-2, E-08193 Bellaterra, Barcelona, Spain*

[3]*Institute of Cosmology and Gravitation, University of Portsmouth, Portsmouth PO1 3FX, UK*
[4]*Department of Physics, Stanford University, 382 Via Pueblo Mall, Stanford, CA 94305, USA*
[5]*Kavli Institute for Particle Astrophysics and Cosmology, PO Box 2450, Stanford University, Stanford, CA 94305, USA*
[6]*Institut de Física d'Altes Energies, Universitat Autònoma de Barcelona, E-08193 Bellaterra, Barcelona, Spain*
[7]*Institute of Astronomy, University of Cambridge, Madingley Road, Cambridge CB3 0HA, UK*
[8]*Kavli Institute for Cosmology, University of Cambridge, Madingley Road, Cambridge CB3 0HA, UK*
[9]*Centre for Theoretical Cosmology, DAMTP, University of Cambridge, Wilberforce Road, Cambridge CB3 0WA, UK*
[10]*Department of Physics and Astronomy, University of Pennsylvania, Philadelphia, PA 19104, USA*
[11]*Center for Cosmology and Astro-Particle Physics, The Ohio State University, Columbus, OH 43210, USA*
[12]*Brookhaven National Laboratory, Bldg 510, Upton, NY 11973, USA*
[13]*Jodrell Bank Center for Astrophysics, School of Physics and Astronomy, University of Manchester, Oxford Road, Manchester M13 9PL, UK*
[14]*Argonne National Laboratory, 9700 South Cass Avenue, Lemont, IL 60439, USA*
[15]*Cerro Tololo Inter-American Observatory, National Optical Astronomy Observatory, Casilla 603, La Serena, Chile*
[16]*Department of Physics and Astronomy, University College London, Gower Street, London WC1E 6BT, UK*
[17]*Department of Physics and Electronics, Rhodes University, PO Box 94, Grahamstown 6140, South Africa*
[18]*Fermi National Accelerator Laboratory, PO Box 500, Batavia, IL 60510, USA*
[19]*CNRS, UMR 7095, Institut d'Astrophysique de Paris, F-75014 Paris, France*
[20]*Sorbonne Universités, UPMC Univ Paris 06, UMR 7095, Institut d'Astrophysique de Paris, F-75014 Paris, France*
[21]*SLAC National Accelerator Laboratory, Menlo Park, CA 94025, USA*
[22]*Laboratório Interinstitucional de e-Astronomia - LIneA, Rua Gal. José Cristino 77, Rio de Janeiro, RJ 20921-400, Brazil*
[23]*Observatório Nacional, Rua Gal. José Cristino 77, Rio de Janeiro, RJ 20921-400, Brazil*
[24]*Department of Physics, University of Illinois, 1110 W. Green St., Urbana, IL 61801, USA*
[25]*National Center for Supercomputing Applications, 1205 West Clark St., Urbana, IL 61801, USA*
[26]*School of Physics and Astronomy, University of Southampton, Southampton SO17 1BJ, UK*
[27]*Faculty of Physics, Ludwig-Maximilians-Universitaet, Scheinerstr. 1, D-81679 Muenchen, Germany*
[28]*Excellence Cluster Universe, Boltzmannstr. 2, D-85748 Garching, Germany*
[29]*Jet Propulsion Laboratory, California Institute of Technology, 4800 Oak Grove Dr., Pasadena, CA 91109, USA*
[30]*Department of Astronomy, University of Michigan, Ann Arbor, MI 48109, USA*
[31]*Department of Physics, University of Michigan, Ann Arbor, MI 48109, USA*
[32]*Kavli Institute for Cosmological Physics, University of Chicago, Chicago, IL 60637, USA*
[33]*Department of Astronomy, University of California, Berkeley, 501 Campbell Hall, Berkeley, CA 94720, USA*
[34]*Lawrence Berkeley National Laboratory, 1 Cyclotron Road, Berkeley, CA 94720, USA*
[35]*Max Planck Institute for Extraterrestrial Physics, Giessenbachstrasse, D-85748 Garching, Germany*
[36]*Department of Physics, The Ohio State University, Columbus, OH 43210, USA*
[37]*Australian Astronomical Observatory, North Ryde, NSW 2113, Australia*
[38]*George P. and Cynthia Woods Mitchell Institute for Fundamental Physics and Astronomy, and Department of Physics and Astronomy, Texas A&M University, College Station, TX 77843, USA*
[39]*Departamento de Física Matemática, Instituto de Física, Universidade de São Paulo, CP 66318, CEP 05314-970 São Paulo, SP, Brazil*
[40]*Department of Astrophysical Sciences, Princeton University, Peyton Hall, Princeton, NJ 08544, USA*
[41]*Institució Catalana de Recerca i Estudis Avançats, E-08010 Barcelona, Spain*
[42]*Department of Physics and Astronomy, Pevensey Building, University of Sussex, Brighton BN1 9QH, UK*
[43]*Centro de Investigaciones Energéticas, Medioambientales y Tecnológicas (CIEMAT), E-28040 Madrid, Spain*

This paper has been typeset from a TEX/LATEX file prepared by the author.